Electrochimica Acta 459 (2023) 142586

Contents lists available at ScienceDirect

Electrochimica Acta

journal homepage: www.journals.elsevier.com/electrochimica-acta

Understanding reactivity of self-assembled monolayer-coated electrodes: SAM-induced surface reconstruction

Francisco W.S. Lucas [a,b], Nathanael C. Ramos [a,b], Daniel K. Schwartz [a], J. Will Medlin [a], Adam Holewinski [a,b,*]

[a] Department of Chemical and Biological Engineering, University of Colorado, Boulder, CO 80303, United States
[b] Renewable and Sustainable Energy Institute, University of Colorado, Boulder, CO 80303, United States

ARTICLE INFO

Keywords:
Lead underpotential deposition
Formic acid oxidation
A,β-unsaturated carbonyl
Surface reconstruction
Electrocatalysis
Self-assembled monolayer

ABSTRACT

Thiolate self-assembled monolayers (SAMs) are often used to modify surface properties, including catalytic activity. These SAMs can also induce reconstruction of some metallic surfaces. Here we show, through formation and subsequent removal of thiolate SAMs from Au polycrystalline electrocatalysts, that irreversible changes to the underlying metal surface can lead to significant changes in catalytic properties, irrespective of specific interactions that might occur between thiolate molecules and various reactants. Using underpotential deposition of Pb as a surface probe, we find that across a range of different thiolates, SAMs tend to increase the proportion of (111)-facets on Au, but they simultaneously increase the defect density upon these and other facets. These changes generally lead to delayed onset but higher maximum activity toward formic acid oxidation, which is hypothesized to relate to changes in both the density of appropriate active site ensembles and interactions of intermediates and site-blocking hydroxyl species with newly generated defects. The impacts of reconstruction are further illustrated through measured shifts in selectivity for electroreduction of crotonaldehyde, with reconstructed catalysts changing the favored product from butanal to crotyl alcohol. Thus, complex surface reorganization may play a significant role in the catalytic behaviors of SAM-modified surfaces.

1. Introduction

Metallic substrates modified by thiolate-based self-assembled monolayers (SAMs) have been used in diverse technological applications including molecular electronics, biotechnology, and for modification of various surface properties [1,2]. They have also been used to modify reactivity and selectivity toward thermo- and electro-chemical catalyzed surface reactions [3–9]. Thiolate SAMs can be deposited on different metallic surfaces by gas-phase or liquid-phase adsorption of precursors such as thiols, disulfides, or thioalkoxide salt solutions. It has been shown that the final (equilibrium) saturation coverage and corresponding SAM structure do not depend on the preparation method [10]. Thus, on a perfectly flat and defect-free surface, the configuration of a SAM tends toward a dense, organized upright arrangement as the thiol concentration/dose or adsorption time increases. The evolution and geometry of these structures are driven mainly by the stabilization resulting from van der Waals (vdW) interactions between adjacent adsorbed molecules [1,2]. However, in addition to the molecular phenomenon of self-organization, it has also been demonstrated that, on some surfaces, the adsorption of thiol molecules can cause considerable reorganization or reconstruction of the surface itself.

On Au(111), for example, thiol-induced reconstruction is associated with formation of atomic vacancies (V_{Au}) and corresponding gold adatom-thiolate complexes ($(RS)_x$–Au_{ad}, $x = 1 - 4$), where the Au_{ad} species is generally bonded to threefold hollow sites on the underlying Au(111) substrate [11]. Increasing coverage (θ) of the thiol promotes increasing degrees of surface reconstruction [12]. For linear alkanethiolate-based SAMs, $(RS)_2$–Au_{ad} species are mainly formed, with a thiolate saturation surface coverage of 0.33. This requires an Au_{ad} coverage of 0.16 [13], which may mainly be provided by removal from step edges [14], but also by the uptake of Au surface atoms from terraces or uplifted islands/defects [1,2], depending on the location and mechanism of thiolate adsorption. Atomic vacancies (V_{Au}, $\theta_{vac} \approx 0.12$)[13,14] can later coalesce to form vacancy islands at terraces or diffuse to yield serration-like steps [14,15]. A more complex dynamic is observed for thiols with terminal groups distinct from alkyl. As examples, thiophenol

* Corresponding author.
E-mail address: adam.holewinski@colorado.edu (A. Holewinski).

https://doi.org/10.1016/j.electacta.2023.142586
Received 4 March 2023; Received in revised form 6 May 2023; Accepted 11 May 2023
Available online 14 May 2023

(PhSH)[16] and 4-mercaptopyridine (4MPy)[17] form ordered SAMs with lower surface saturation coverage, $0.2 < \theta < 0.25$. Whereas alkanethiolate-based SAMs show both V_{Au} and Au_{ad}, V_{Au} and vacancy islands have not been observed on Au(111) reconstructed by PhSH-SAMs, and only isolated V_{Au} have been found for 4MPy-SAMs [17, 18].

While reconstruction phenomena have been studied on Au (and many other metals)[1] extensively using high-resolution STM, only flat, nearly defect-free, and generally single-crystalline surfaces have been studied. Little is known about the dynamics and progression of reconstruction on polycrystalline surfaces—for example, whether native defects are etched or modified, and the extent to which edges and kinks are modified relative to terraces, remain open questions. It may nonetheless be expected that reorganization phenomena occur and could influence the chemical reactivity of the surface.

In the context of catalysis, thiols present in the substrate/SAM system can have different functions: (i) they can be the actual catalytic sites by anchoring a catalytic head group—this motif has been successfully employed on a multitude of reactions[19]—or, (ii) they can tune the interface environment and/or underlying catalyst surface reactivity. For example, steric impediment of specific sites (terraces vs. edges) and interaction between thiols and reactants have been found to influence the adsorption geometry of reactants on catalytic sites, promoting substantial selectivity shifts for various (thermo)catalytic reactions [3, 20–25]. Examples in electrocatalysis have also recently been increasingly reported. Enhancement of formic acid oxidation has been observed on Au(111) electrodes modified with 4-mercaptopyridine SAM [4]. The improvements were suggested to relate to changes in local hydrophobicity promoted by the presence of thiol, as well as interactions (acid--base and electrostatic) between thiol and reactants/intermediates [4]. In addition, diverse examples of the catalytic effects promoted by SAMs have been shown for the CO_2 reduction reaction, where the selectivity and activity have been proposed to be affected by CO_2 gas trapping in the hydrophobic thiol layer [7], dipole interaction between thiols and adsorbed intermediates on the catalytic surface [8], and/or stabilization of a cationic-state of the metallic substrate [9]. Similar phenomena have also been invoked with respect to electrocatalytic nitrogen reduction [5, 6].

Despite widespread examples where coating catalysts with thiol-SAMs has promoted interesting catalytic behaviors, a remaining unexplored question involves the degree to which reconstruction may contribute to observed catalytic differences. Even in cases where the sulfur content on the catalyst is unaltered during the reaction, the SAM structure may be dynamic or the reaction may occur on reconstructed thiol-free regions present on SAM-coated catalysts. Herein, we analyze SAM-induced surface reconstruction on polycrystalline Au surfaces by deposition and subsequent removal of thiol SAMs. The surface facet distribution and defect morphology are probed through underpotential-deposited Pb-stripping experiments, where SAMs are found to increase the population of (111)-surface domains while also increasing the density of defects within those domains. We then explore how the changes in surface structure impact two reactions: oxidation of formic acid (which is known to be sensitive to various surface facets and defects), and the reduction of crotonaldehyde, an α,β unsaturated carbonyl compound for which selectivity in reduction is critical and could be influenced by reconstruction phenomena. Formic acid oxidation is found to have a later onset but higher maximum activity on reconstructed surfaces, while crotonaldehyde reduction exhibits significant shifts in product selectivity due to reconstruction.

2. Experimental

2.1. Materials and chemicals

All analytical grade chemicals were obtained from Sigma-Aldrich (when not specified) and used directly without further purification. Sodium thiomethoxide (precursor of methanethiol, C1SH, 95%), 1-Propanethiol (C3SH, 99%), 1-Hexanethiol (C6SH, 95%), 1-Adamantanethiol (AdmT, 95%), Thiophenol (PhSH, 97%), 4-Mercaptopyridine (4MPy, 95%), anhydrous ethyl alcohol (≥ 99.5%), NaOH (99.995% trace metals basis), $NaClO_4$ (>99.9%), $Pb(ClO_4)_2$ (> 98%), $NaHCO_3$ (> 99.5%), Suprapure $HClO_4$ (> 99.999%), NaH_2PO_4 (Synth, >95%), Na_2HPO_4 (Synth, >95%), formic acid (≥ 95%), crotonaldehyde (≥ 99%, predominantly trans, 0.1–0.2% BHT and 1% H2O as stabilizers), crotyl alcohol (≥ 96%, *cis* and trans mixture), butyraldehyde (≥ 96%), 1-Butanol (anhydrous, ≥ 99.8%), 0.05 wt.% sodium 3-(trimethylsilyl)−2,2,3,3-tetradeuteropropionate (TMSP) in D_2O (99.9 at.% D), Argon (UHP, Airgas Inc.). Au plate (Goodfellow, 0.25 mm thickness, 99.99% purity), Au wire (Goodfellow, 0.75 mm diameter, ≥99.95% purity), ultra-pure deionized water (specific resistance >18.2 MΩ cm, Elga Purelab Flex water purification system) was used to prepare all solutions.

2.2. Electrochemical experiments

Electrochemical experiments were carried out using a potentiostat/galvanostat (Gamry Instruments, Reference 3000). Two different three-electrode cells were used for specific experiments: a conventional H-type cell and a homemade μ-cell (more details can be found in Supporting Information, Fig. S1). The H-cell had cathodic and anodic compartments of 10 mL each, while the μ-cell had compartments of 450 μL. For both cells, the compartments were separated by a proton- or anion-exchange membrane (Fuel Cell Store Nafion® 117 or Fumapem® FAA-3–50, respectively), depending on pH. A leak-free $Ag/AgCl/Cl^-_{(sat.\ KCl)}$ or $Hg/HgO_{(0.1\ M\ NaOH)}$ (for experiments at pH 13) electrode was used as the reference electrode (RE), and Au plates or wires were used as auxiliary electrodes (AE). A reversible hydrogen electrode (RHE) was used to calibrate the RE, and all potentials in this work are referenced to RHE, unless otherwise noted. Uncompensated resistance (R_u) was measured by current interrupt and/or electrochemical impedance spectroscopy (EIS), and all measurements were R_u corrected. The systems were degassed with $Ar_{(g)}$ and the H-cell temperature was controlled by a thermostatic bath (Fisher Scientific).

2.2.1. Self-assembled monolayer formation, and electrochemical characterization and removal

Six different thiolate self-assembled films were grown on Au electrodes at room temperature from ethanolic thiol solutions, with concentrations of 1 or 5 mM. Before the deposition process, the Au surface was, sequentially, cleaned in perchloric-piranha solution (PP-cleaning), flame polished, electrochemically polished, and soaked in anhydrous ethanol for 5 min (for surface conditioning and removal of remaining AuO_x)[26] —additional details can be found for individual cases below. Then, the substrate was transferred to the respective fresh-prepared ethanolic thiol solution and left soaking for 30 min at room temperature. After the self-assembly process, the electrode (Au-SAM) was vigorously rinsed with pure ethanol (for elimination of non-chemically bound thiols) and immediately used for electrochemical experiments. The thiols used in this work were (structures shown in Supporting Information, Fig. S2): Methanethiol (C1SH), 1-propanethiol (C3SH), 1-hexanethiol (C6SH), 1-adamantanethiol (AdmT), thiophenol (PhSH), and 4-mercaptopyridine (4MPy). A control sample, referred to as "unreconstructed-Au (ur-Au)" was also submitted to the same preparation process, except without the deposition in thiol solution.

Electrochemical desorption of thiols (reductive stripping) was characterized by linear sweep voltammetry (LSV) in 0.1 M NaOH (as supporting electrolyte, pH 13) at a scan rate of 20 mV s^{-1} and potential window from −0.3 to −1.4 V vs. $Ag/AgCl_{(sat\ KCl)}$. The voltammograms can be seen in the Supporting Information (Fig. S3) and show that all the thiols used in this work can be electrochemically stripped prior to reaching −1.4 V vs. $Ag/AgCl_{(sat\ KCl)}$. This was further confirmed by XPS measurements shown in Fig. S6. Thus, the removal of the thiols from the

Au surfaces was performed potentiostatically by polarizing the electrode at −1.4 V vs. $Ag/AgCl_{(sat\ KCl)}$ for 2 min in 0.1 M NaOH under vigorous Ar bubbling and mechanical stirring; this facilitates mass transport of the thiols away from the electrode and eliminates re-adsorption. These electrodes will be called "reconstructed (r-)" from now on in the text. It is worth emphasizing here that "reconstructed electrodes", in this context, are thiol-free/sulfur-free electrodes with surface reconstruction induced by SAM adsorption and retained after electrochemical removal of the SAM. While it is challenging to determine the extent to which reconstructions may evolve further during potential cycling, it has nonetheless been demonstrated that Au surfaces continue to exhibit structural differences (relative to pristine Au) after electrochemical removal of thiols (i.e., Au_{ad} and V_{Au} defects are still present on the surface) [14,27,28]. This stands in contrast to thermal desorption of SAMs, where defects have higher mobility and can be diminished by annealing processes [29].

To determine the electrochemical surface area (ECSA), capacitance measurements were calibrated against Au surface oxide reduction. The reason that the oxide reduction peak could not be used directly is that high oxidizing potentials can alter the surface in comparison to what is formed by interactions with the SAMs. For this experiment, electrodes were first cleaned by electropolishing in 0.1 M $HClO_4$ (pH 1) by cycling 50 times from 0.5 to 1.7 V vs. RHE, at 300 mV s^{-1}. Then, the ECSAs of eight (8) different ur-electrodes were measured by integrating the charge of the AuO_x reduction peak (where 390 μC is equivalent to 1 cm^2) [30] from cyclic voltammograms (CV) collected in 0.1 M $HClO_4$ (pH 1) from 0.24 to 1.44 V vs. $Ag/AgCl_{(sat\ KCl)}$ (0.5 to 1.7 V vs. RHE) at 20 mV s^{-1}. The respective specific capacitance of each electrode was also measured in the same supporting electrolyte using CVs collected between 0.3 to 0.7 V vs. $Ag/AgCl_{(sat\ KCl)}$— the pure capacitive region— at different scan rates (50, 100, 150, 200, 250, and 300 mV s^{-1}). The voltammograms and plots of capacitance vs. scan rate for this experiment can be seen in the Supporting Information (Fig. S4). The relationship between capacitance at 0.5 V and ECSA obtained from the polycrystalline Au electrodes was 32.4 ± 2.6 (n = 8) μF cm^{-2}_{ECSA}. From this method, complete thiol removal was confirmed before every experiment [34]—see Figs. S5 and S9.

2.2.2. Lead underpotential deposition

For lead underpotential deposition (Pb-UPD) experiments, a Au-bead electrode was used. To make this electrode, a gold wire (Goodfellow, 0.75 mm diameter, ≥99.95% purity) was cleaned for ca. 30 min in hot perchloric-piranha solution (PP-cleaning, 3 parts concentrated $HClO_4$ to one part 30% H_2O_2 by volume) followed by rinsing with ultrapure water and ultrasonication for 5 min. After PP-cleaning, the wire was melted into a spherical bead of approximately 2.5 mm in diameter and left to slowly cool in the air (room temperature of 18 °C) for 1 min before being rinsed with ultrapure water. To improve reproducibility and simulate the treatment done on Au plates used in electrolysis experiments (crotonaldehyde reduction further below), the bead electrode was always submitted to PP-cleaning, flame polishing and electropolishing between each experiment with thiols.

Pb-UPD experiments were performed on ur- and r- electrodes (six different thiolate-SAM depositions for reconstruction). An oxygen-free H-cell was used, and a Pb-UPD monolayer was potentiostatically deposited at −0.4 V vs. $Ag/AgCl_{(sat\ KCl)}$ for 1 min from a solution containing 0.1 M $NaClO_4$, 0.01 M $HClO_4$, and 0.001 M $Pb(ClO_4)_2$, following well-established procedures [31,32]. Stripping linear sweep voltammograms were collected at a scan rate of 20 mV s^{-1}, from −0.4 to 0.4 V vs. $Ag/AgCl_{(sat\ KCl)}$. Stripping peaks were deconvoluted using Gaussian functions and can be observed in the Supporting Information (Fig. S7).

2.2.3. Electro-oxidation of formic acid

The formic acid oxidation reaction (FAOR) was performed on ur- and r- Au-bead electrodes, prepared identically to the description for Pb-UPD experiments. Each electrode was studied by cyclic voltammograms collected in 0.1 M $HClO_4$ + 0.1 M HCOOH, from 0 to 1.2 V vs. RHE, at a scan rate of 20 mV s^{-1}, in an H-cell. Differential electrochemical mass spectroscopy (DEMS) was also used to confirm CO_2 production and probe the possible production of H_2 during FAOR, since several works have demonstrated small amounts of H_2 production from FA on other metals [33]. DEMS experiments were only performed on ur-Au in the μ-cell. For these tests, an Au film was deposited on a gas diffusion layer and, using an MS capillary probe, the μ-cell was coupled to the quadrupole vacuum system of a Hiden HPR40 mass spectrometer during LSV and pulsed-potential experiments (more details can be found in Supporting Information, Fig. S8). An electron energy of 70 eV and emission current of 700 μA were used for ionizing all species. A scanning electron multiplier (multiple ion detection mode) with a multiplier voltage of 1.4 kV was applied to simultaneously detect H_2 (m/z = 2) and CO_2 (m/z = 44).

2.2.4. Electro-reduction of crotonaldehyde

The electrochemical reduction of crotonaldehyde (CRAL) was initially performed in a gas-tight H-cell with headspace sampling by gas chromatography. After verifying H_2 and other gasses were negligible (Fig. S10 Supporting Information), a μ-cell was utilized for electrolyses, with Au-plates (ur- and r-) used as working electrodes. These plates were mechanically polished with alumina slurry (0.05 μm, Allied High Tech Products Inc.) to a mirror-like finish, followed by ultrasonic cleaning (in ultrapure water and ethanol for 5 min each) to remove residual alumina. Then, similarly to what was done to the Au-bead electrodes, the plates were subjected to flame polishing, electropolishing, and ethanol soaking. The reconstruction induced by thiolate-SAMs was created using the same procedure mentioned in previous sections (i.e., thiol deposition and removal, followed by capacitance check to make sure the surface was thiol-free[34]—see Fig. S5).

A quick pH and electrolyte screening was first performed using LSV as an optimization guide. Then, electrolyses were performed at four different potentials (−0.55, −0.70, −0.85, and −1.00 V vs. RHE) and two different charges (1 and 2 F per mol of CRAL), using an initial CRAL concentration of 50 mM. Based on these exploratory experiments (data and discussion are presented in the Supporting Information), electrocatalytic studies were performed with ur- and r- electrodes in 0.1 M $NaClO_4$ + 0.1 M $NaHCO_3$ (buffered pH 8) as the supporting electrolyte, at −0.70 V vs. RHE and room temperature, passing a total charge of 1F per mol of CRAL (i.e., 2.17 C for 450 μL of 50 mM CRAL). The product analysis was performed by ^{1}H NMR and liquid chromatography (LC); analytical procedure details are organized in the Supporting Information (and Figs. S11–S13). For NMR analysis, a Bruker AVANCE-III 400 MHz NMR spectrometer was used, and LC analyses were performed on an Advion 2000 HPLC equipped with a 300 mm x 6.5 mm sulfonated polystyrene gel column (Hi-Plex H, Agilent) and a UV diode array detector (DAD).

3. Results and discussion

3.1. Signatures of reconstruction from lead underpotential deposition

Direct measurement of surface reconstruction on Au particles, e.g. via microscopy, is challenging. A more straightforward approach is to use indirect probes of the distribution of surface sites. It has been well-established that the phenomenon of underpotential deposition (UPD) is very sensitive to the crystalline structure of the substrate surface. Lead-UPD and its subsequent monolayer stripping have been extensively studied on Au, Ag, Cu, and Pt single- and poly-crystalline surfaces [35,36]. For this reason, Pb-UPD was chosen as a probe for studying the surface reconstruction of polycrystalline Au caused by SAM deposition. Reconstruction was studied with six different thiols: Methanethiol (C1SH), 1-propanethiol (C3SH), 1-hexanethiol (C6SH), 1-adamantanethiol (AdmT), thiophenol (PhSH), and 4-mercaptopyridine (4MPy). Capacitance and XPS measurements performed before and after SAM

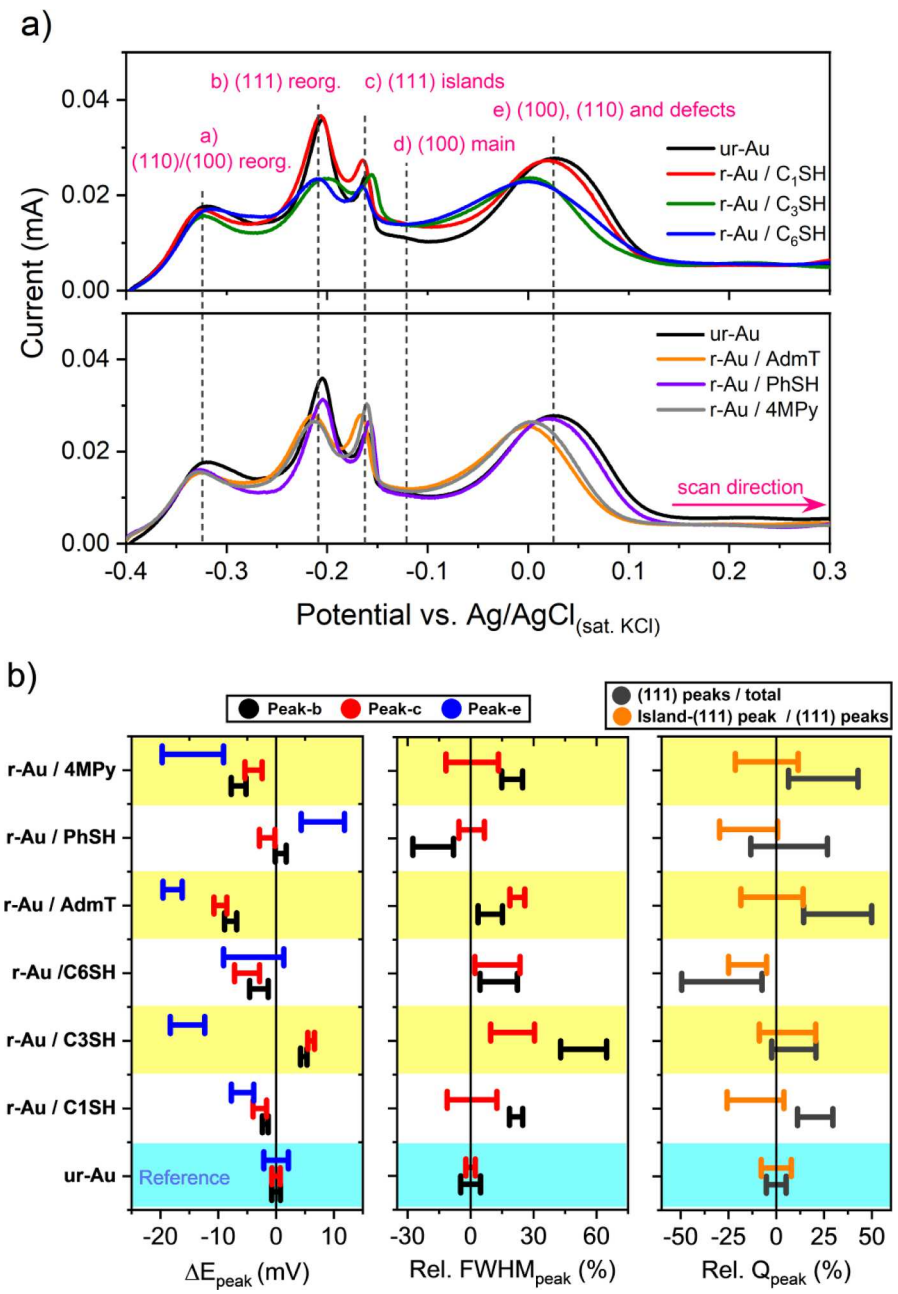

Fig. 1. Pb-UPD adlayer desorption experiments on different polycrystalline Au surfaces (unreconstructed, ur-, and reconstructed, r-) by different thiol-SAMs after deposition and removal: a) stripping linear sweep voltammograms after Pb monolayer was grown at −0.4 V for 60 s, and b) relative peak potential shifts ($\Delta E_{peak} = E_{peak} - E_{peak}$ [ur-Au]), full widths at half maximum (Rel. $FWHM_{peak} = FWHM_{peak} / FWHM_{peak}$ [ur-Au]), and peak-charges (Rel. $Q_{peak} = Q_{peak} / Q_{peak}$ [ur-Au], where Q_{peak} is defined by the charge fraction [peak-*b* + peak-c] / [total] for (111) peaks or [peak-c] / [peak-*b* + peak-c] for (111)-islands).

removal on the reconstructed surfaces showed that the thiols were completely removed by voltammetric stripping prior to UPD, as discussed in the Experimental section and the Supporting Information (Figs. S5 and S6). Linear sweep voltammograms (LSVs) of Pb-UPD monolayer stripping were collected on each unreconstructed (ur) and reconstructed (r) polycrystalline Au surface and are shown in Fig. 1a.

Five main Pb-adlayer stripping peaks are observed and labeled as follows: (a) with peak potential (E_{peak}) ca. −0.32 V, (b) at ca. −0.21 V, (c) at ca. −0.16 V, (d) a small shoulder at ca. −0.12 V (more evident in ur-Au), and (e) between 0 and 0.03 V, all vs. Ag/AgCl(Sat. KCl). Peak-a is known to be partial stripping from very compact adlayers formed with a reorganization of Pb adatoms already deposited at less negative potentials on (110) and (100) terraces [31,32]. This reorganization, which compresses the adlayers and accommodates extra adatoms, does not happen on wide (111)-terraces (at least 6 atoms wide). Peak-b and peak-c next correspond to the stripping of Pb from the (111)-terraces, which begins with coverage of roughly 0.9. Thermodynamic and kinetic effects make the (111)-adlayer, present before the stripping at peak-b, convert into stable Pb-islands that are next stripped at peak-c [31,32,35]. The presence of peak-c is thus associated with large, extended (111)-facets [37–40]. Finally, peak-d is associated with the majority of stripping from (100)-terraces [31,32,41], while the broad peak-e is composed of several processes, including removal of some residual Pb on (100)-surfaces, stripping from (110)-facets, and steps and kinks on various faces. Contributions from atomic defects (e.g., vacancies and adatoms) have not been systematically probed in past studies [31,32], but we expect that scattered atomic defects most distinctively lead to broadening of the signature peaks for the various faces upon which they form.

To evaluate differences between r- and ur-surfaces, Fig. 1b shows relative changes in peak potential (ΔE_{peak}), full widths at half maximum ($FWHM_{peak}$), and integrated peak charges (Q_{peak}) relative to ur-Au. These metrics come from deconvolution of all peaks present in the stripping signatures with Gaussian functions, as shown in the Supporting

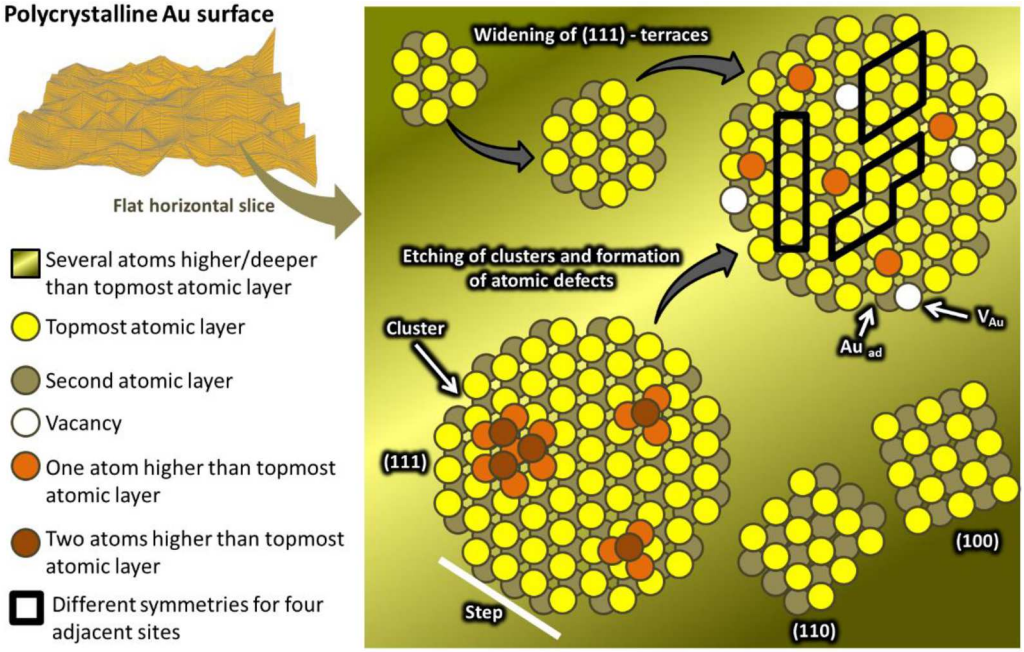

Fig. 2. Schematic representation of hypothesized surface reconstruction effects.

Information, Fig. S7 and Table S1. To also help visualize effects created by reconstruction, Fig. 2 schematically shows a variety of structural motifs that will be referenced below.

The combined analysis of UPD data shown in Fig. 1b suggests that reconstruction via thiolate deposition and stripping results in an increased prevalence of defect-laden (111) terraces with a broad size distribution. First, observing ΔE_{peak} values in the left frame in Fig. 1b, the modest variation (< 10 mV) for peak-b and peak-c (Pb_{ad} on (111)-terraces) suggests that changes in defects on the (111)-terraces (promoted by reconstruction) do not significantly affect the average stripping energy of Pb-islands or Pb-full-adlayers on these facets relative to ur-Au. However, as shown in the right frame of Fig. 1b, the relative stripping charge (rel. Q_{peak}, defined by fraction of total charge for a peak, normalized to the same quantity on ur-Au) for the sum of peak-b and peak-c (the (111) peaks) increases for almost all reconstructed surfaces (all except for C6SH, which forms the most ordered and stable SAM among all thiols studied in this work). This suggests that (111)-terraces are extended/created by etching large native defects (e.g. uplifted steps or clusters/islands) and/or relocating atoms to add to (111)-domains, as depicted in Fig. 2. Despite the increased charge associated with (111)-facets, there is also a general growth in $FWHM_{peak}$ values for peak-b and peak-c (center frame in Fig. 1b); these grow for all explored thiols except PhSH, which yields some narrowing in peak-b. Peak broadening can be considered an indicator of a widening distribution of ensemble sizes (number of atoms composing the continuous domains), and/or the existence of more atomic defects upon those ensembles. Thus, combining both Q_{peak} and $FWHM_{peak}$ for the (111)-domain features, the data suggest a general increase in the total quantity of (111)-terrace domains, although it cannot alone reveal whether their size distribution widens, the density of vacancies or adatoms grew, or a combination of these options occurred. The $FWHM_{peak}$ for peak-c is less affected than peak-b since peak-c is associated with stripping of Pb islands (e.g., at the center of (111)-terraces); the initiation events that cause peak-b would be more variable with the creation of more Au_{ad} and/or V_{Au} species by reconstruction. Moving to peak-d and peak-e in Fig. 1, ΔE_{peak} values are associated with the character and density of surface steps, kinks, and defects present outside of the (111)-terrace domains (peak-d mainly varying due to interference from peak-e). Although it is not possible to deconvolute and specify all types of defects sampled in this feature, it is evident from the ΔE_{peak} of peak-e that reconstruction by different thiols causes distinct and complex restructuring dynamics outside of the (111)-terraces (shifting distributions of defect types and relative degrees of facet exposure). C3SH and AdmT promoted these effects to the greatest degree, based on their outsized influence on peak-e.

In summary, SAM-induced reconstruction generally appears to increase the total surface area contribution of (111)-terrace domains. It also changes either the distribution of domain sizes, or (as will be argued below) the nature and distribution of defects across all domains. AdmT made the total quantity of (111)-terraces increase the most (AdmT > 4MPy > C1SH > C3SH ≈ PhSH > ur > C6SH, from Q_{peak}), while C3SH promoted the most dispersion in the (111)-associated stripping processes (C3SH > C1SH ≈ 4MPy > C6SH ≈ AdmT > ur > PhSH, from $FWHM_{peak}$). C3SH, AdmT, and 4MPy promoted the highest degree of restructuring outside of (111)-terraces (based on ΔE_{peak} for peak-e). While deconvoluting the contribution of each existent face or group of defects in finer detail from Pb-UPD is difficult, the changes in the overall stripping profiles themselves are strong evidence for the complex surface reorganization promoted by different thiolate-SAMs. These must, in turn, affect the catalytic properties of the respective surfaces. This is explored in the following two sections.

3.2. Formic acid oxidation

The electrochemical formic acid oxidation reaction (FAOR) is known to be most rapid on (111)-terraces of Au [42,43], so it would be expected that SAM-induced restructuring should impact the specific activity of Au for FAOR. Fig. 3a shows CVs for FAOR on ur-Au and r-Au surfaces, with a comparison of extracted metrics compiled in Fig. 3b (also provided in tabular form in Table S2): (i) relative peak potential shifts (ΔE_{peak}) vs. ur-Au; (ii) "onset" potential shift, defined as the relative overpotential (ΔE vs. ur-Au) to reach current density 10 μA/cm^2; (iii) relative rate at 1.00 V (rel-R_{FAOR}, the ratio between current density for r-Au catalysts and ur-Au at its E_{peak}, 1.00 V); and (iv) hysteresis factor (potential span between forward and backward scan at half maximum current density, $HE_{M/2}$). A quick analysis of the figure makes clear that all r-surfaces show small positive ΔE at i = 10 μA cm^2_{ECSA} (delayed onset), but generally have much higher rel-R_{FAOR} values. We stress that the upper

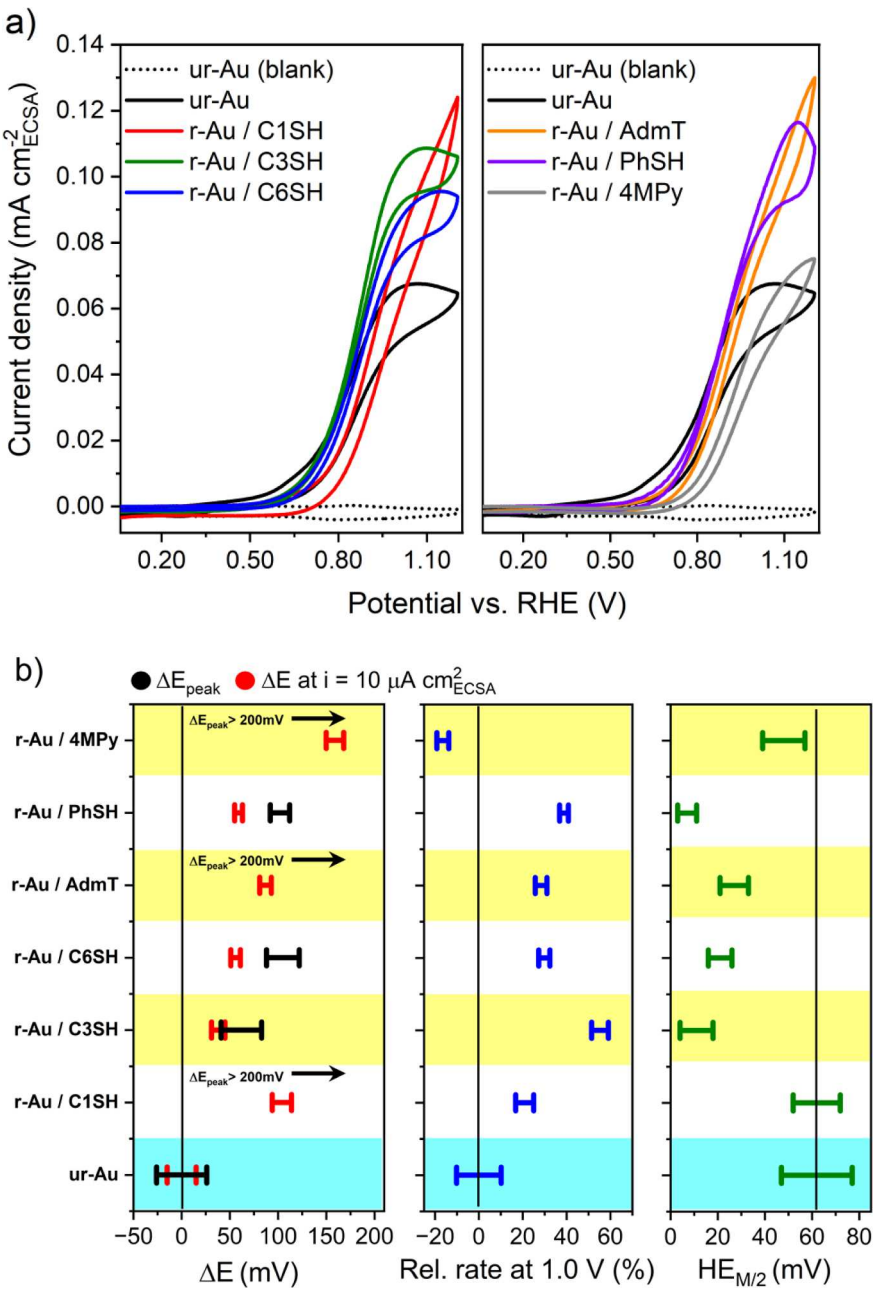

Fig. 3. a) Cyclic voltammograms for formic acid oxidation on different polycrystalline Au surfaces at a scan rate of 20 mV s^{-1} in 0.1 M $HClO_4$ + 0.1 M HCOOH solution. b) Shifts for peak potential (ΔE_{peak}, where applicable) and potential at a current density of 10 μA cm^{-2} (left), relative rate at 1.00 V (center), and hysteresis factor (potential span between forward and backward scan at half maximum current density, $HE_{M/2}$, right). Labels signify unreconstructed (ur-), and reconstructed (r-) surfaces exposed to different thiol-SAMs (after complete electrochemical removal of the thiol molecules).

potential limit is well below the gold oxide formation potential, so these effects are solely introduced by structural changes created by the adsorption and removal of SAMs. Plateaus and decreases in the current at high potential are also not caused by mass transfer limitations (confirmed with variation of stirring), but rather by competition between the reactant and surface hydroxyl groups that block active sites [42]:

$$H_2O_{(l)} + * \rightarrow e^- + OH_{ad} + H^+_{(sol.)} \quad (1)$$

By comparing UPD features and FAOR profiles, it appears that increasing the quantity of (111)-surface area could contribute to accelerating the reaction, but it cannot fully explain (i) delayed onset potentials, and (ii) that the maximum currents generally grow by larger factors than the gains in (111)-surface area (based on Q_{peak} for peaks b and c).

To help interpret the role of reconstruction, we note that FAOR occurs on Au electrodes *via* a single direct path [42]. The mechanism involves electroadsorption of formic acid dimers, $(HCOOH)_2$, (transferring one electron and one proton per monomer) to yield surface formates ($HCOO_{ad}$). This is followed by a purely chemical, rate-determining bimolecular decomposition reaction between adjacent surface formates, producing one H_2 and two CO_2 molecules for each dimeric unit. This is notably in contrast to FAOR on Pt-group metals, where indirect paths (via CO_{ad} intermediate) can also be present and require participation of OH_{ad} [33]. Two additional electrons are gained from oxidation of H_2, as the potential is generally high above the threshold for that reaction. We confirmed that H_2 gas generation was negligible by DEMS experiments (Supporting Information, Fig. S8). The aforementioned steps are summarized below:

$$(HCOOH)_{2(sol.)} + 4* \rightarrow 2e^- + 2HCOO_{ad} + 2H^+_{(sol.)} \quad (2)$$

$$2HCOO_{ad} \rightarrow 2CO_{2(g,\ sol.)} + H_{2(g,\ sol.)} + 4* \quad (3)$$

$$H_{2(g,\ sol.)} \rightarrow 2e^- + 2H^+_{(sol.)} \quad (4)$$

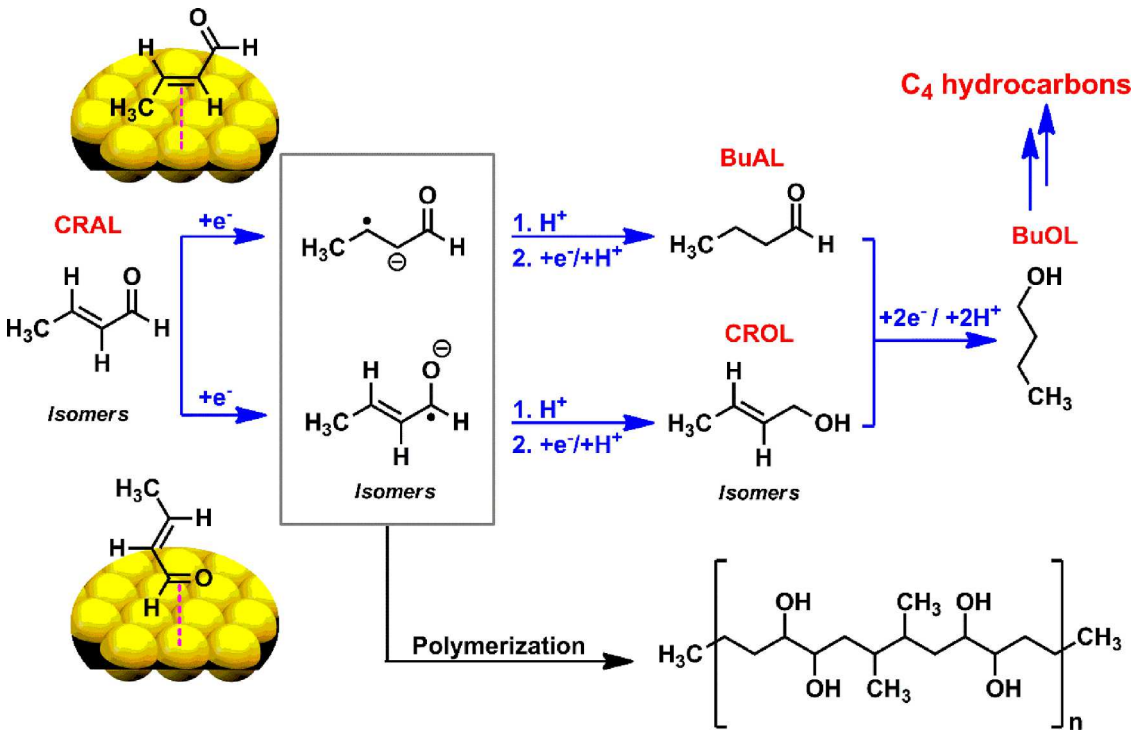

Scheme 1. Electrochemical reduction of crotonaldehyde (CRAL). Adsorption configurations will favor formation of crotyl alcohol (CROL) or butanal (BuAL). Intermediate radical anions (or adsorbed anions) can lead to polymerization side reactions. Homogenous hydrolysis reactions are not shown.

Since bimolecular decomposition (eq. (3)) requires terrace ensembles with at least four sites that can accommodate two adjacent $HCOO_{ad}$, we suggest that the delayed onset behavior of reconstructed catalysts is likely a byproduct of an increase in defect density on the expanded (111)-terraces. Although we cannot comment on the precise geometry or distributions of available ensembles, Fig. 2 illustrates examples of some possible four-site configurations on (111)-terraces. Defects may disrupt site ensembles with appropriate symmetry for $HCOO_{ad}$ pairs to undergo second-order surface reactions. Increased defect density could also directly stabilize formate species and slow their rate of surface diffusion (slowing rate of forming reactive dimers). This could even manifest indirectly through interactions with OH_{ad}, since these species will tend to accumulate at defect sites at low potentials[44,45] and could offer H-bonding stabilization.

At higher potentials that permit rapid adsorption, high coverages of $HCOO_{ad}$ will be reached, removing limitations by the rates of surface diffusion and revealing a maximum rate dictated by competition between the (pure chemical) rate of bimolecular decomposition between adjacent $HCOOH_{ad}$ pairs and growth of the site-blocking OH_{ad} population. The order of maximum FAOR activity at 1.0 V (from rel-R_{FAOR}) is C3SH > PhSH > C6SH ≈ AdmT > C1SH > ur > 4MPy, although C1SH and AdmT continue to increase in current and do not reach a peak prior to the potential region where reconstructions can be damaged at high potential (~1.3 V). The increase in currents for r-catalysts could partly be attributable to higher overall populations of (111)-domains, although we could not fit a strong correlation with any particular metric. 4MPy also presents very different behavior from the other SAMs (addressed below). The poor correlation between (111)-facet area and activity is a challenging result to interpret, but we speculate that either (a) defects can scavenge OH_{ad} species in a manner that increases the available quantity of reaction-capable ensembles on the (111)-terraces, or (b) there can be beneficial adsorbate-adsorbate interactions with OH_{ad} when anchored to defect sites [44,45], which might stabilize a key intermediate or transition state. Neither effect would be seen at low potentials due to the low adsorbate coverages. Regarding the first hypothesis, the adsorption of OH_{ad} to terraces can be probed from the values of ΔE_{peak} (potential where it outcompetes formate) as well as $HE_{M/2}$ (since hysteresis is created by reaching high OH_{ad} coverages and slowing the subsequent desorption on the reverse scan), both given in Fig. 3b. These signatures suggest that all r-surfaces have a lower OH_{ad} coverage on open terraces than ur-Au for any given potential. Regardless of the exact interpretation, rough surfaces are not in general beneficial for FAOR, so it appears that combining (111)-facets with highly dispersed defects may be a key factor in raising the activity.

Summarizing, FAOR reveals significant impacts of reconstruction phenomena promoted by different thiolate-SAMs deposited on polycrystalline Au. Complementing insights from Pb-UPD experiments, we observe that most of the thiols promoted an etching of low-coordinated features and large defects, enlarging (111)-surface ensembles, though likely leaving significant residual defects such as adatoms and vacancies. These defects in turn may lead to a reduction in site ensembles having ideal symmetry for the FAOR (slowing onset), but the larger quantity of terraces and some synergistic benefit to highly dispersed defects apparently raises the rel-R_{FAOR} at high overpotential. A notable exception is that the 4MPy SAM leads to very late onset and low maximum activity, near to ur-Au. 4MPy was the only nitrogen containing SAM, and such compounds are well-known to complex with Au ions; pyridinic SAMs have been documented to cause significant leaching of Au, with predominantly vacancy defects [17,18]. These types of defects (as opposed to adatoms) may be detrimental, or they may reach such a high density that bimolecular reaction steps are impeded even at high reactant surface coverage.

3.3. Electrochemical reduction of crotonaldehyde

The effects of reconstruction were next explored for a reaction with surface-sensitive selectivity. Achieving high selectivity, yield, and faradaic efficiency for (electro)reduction of α,β-unsaturated carbonyl compounds such as (E, Z)−2-butenal (crotonaldehyde, CRAL) is a major challenge. It has been found that CRAL can be unselectively reduced not only to crotyl alcohol (CROL), butyraldehyde (BuAL), and 1-Butanol (BuOL), but also to highly hydrogenated C_4-hydrocarbons (e.g. 1-

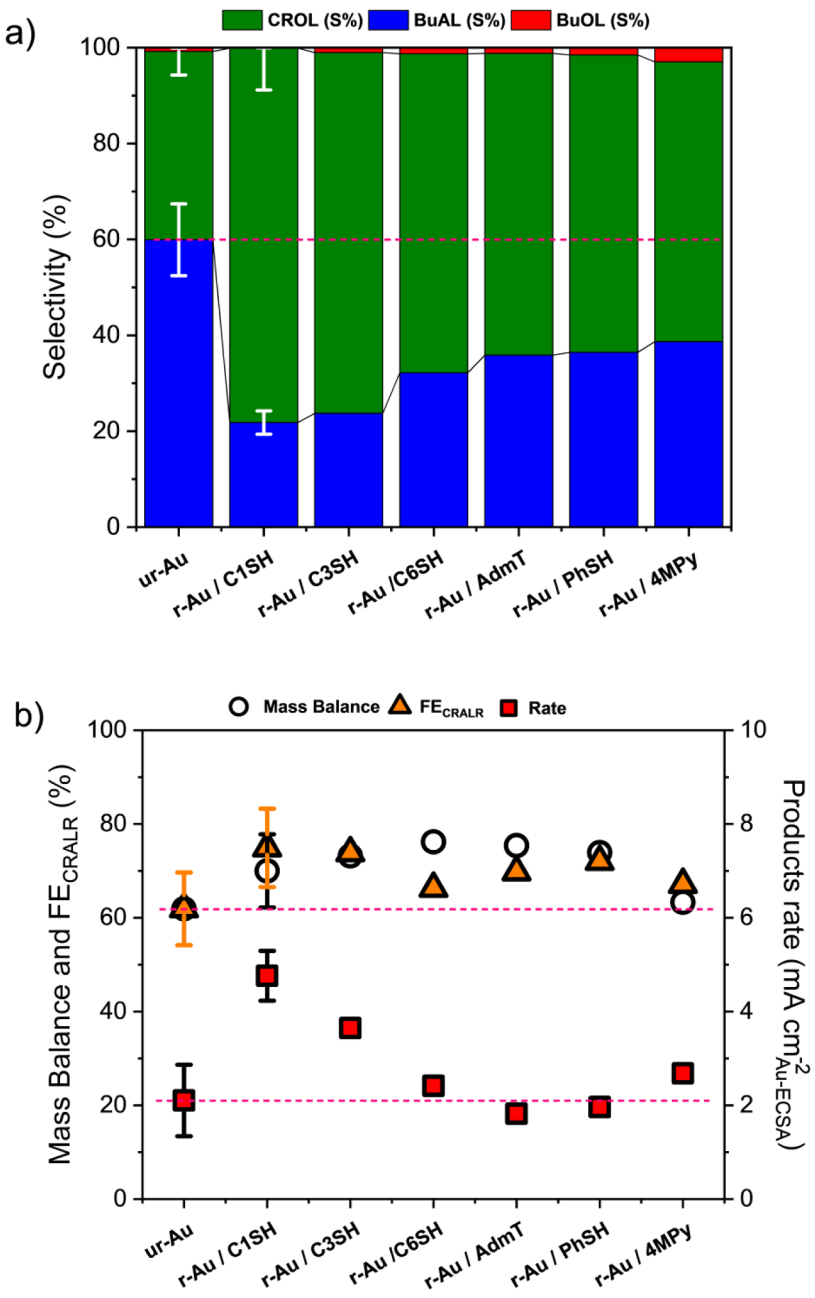

Fig. 4. a) Selectivity, and b) mass balance, faradaic efficiency (FE_{CRALR}), and total product formation rate for CRALR on polycrystalline-Au surfaces, unreconstructed (ur-) and reconstructed (r-) by different thiol-SAMs (after complete electrochemical removal of the thiol molecules). Electrolyses were performed with 50 mM CRAL in 0.1 M $NaClO_4$ + 0.1 M $NaHCO_3$ (buffered pH 8), at −0.70 V vs. RHE (iR-corrected) and room temperature, passing a total charge of 1F per mol of CRAL. Error bars are shown for the most selective surfaces toward either product.

butene, *n*-butane, *cis,trans*-2-butene), as shown in Scheme 1. [46–48] In addition, the mass balance and faradaic efficiency (FE) can be greatly affected by competing polymerization paths and the hydrogen evolution reaction (HER). Under commonly studied conditions, Ni, Co, Cu, Au, Pd, and Pt are all found to be most selective toward BuAL (selectivity over 50%), while Ag is more selective to CROL, and Fe to BuOL. However, in addition to conditions such as supporting electrolyte composition, potential, and charge passage, catalyst surface morphology can also play an important role in the observed selectivity [46].

Part of the challenge in selective reduction of CRAL is that the hybridization of multiple molecular orbitals (some more localized on C = O, others on C = C) with *d*-states from metallic catalysts makes adsorption paths through C = O and C = C both favorable in many cases [49,50]. It has also been discussed that coverage effects (associated with steric and lateral interactions) can make the adsorption mode shift from C = C (lower coverage) to C = O (higher coverage). Because of this complexity and sensitivity toward surface properties, this reaction was chosen to extend the illustration of reconstruction effects toward selectivity.

Based on an optimization of reaction conditions (shown in Supporting Information Section 3), electrocatalytic studies were performed on the ur- and r- electrodes using 0.1 M $NaClO_4$ + 0.1 M $NaHCO_3$ (buffered pH 8) as the supporting electrolyte, applying a constant potential of −0.70 V vs. RHE and passing a total charge of 1F per mol of CRAL. Fig. 4 shows the resulting rates (average over reaction), selectivity, mass balance (MB), and faradaic efficiency (FE) for CRAL reduction on ur- and various r-Au electrodes.

Analyzing Fig. 4, we can clearly see that the reconstruction promoted by thiolate-SAMs impacts CRAL reduction; the selectivity on all r-catalyst shifted 20 − 40% toward CROL compared to the ur-catalyst. Even though very little is known about the reactivity of CRAL on different sites (terraces, edges, kinks, general defects) present on polycrystalline Au, this result suggests that, compared to ur-Au, the r-electrodes have a higher density of sites (per ECSA) that: i) bind CRAL molecules through

C = O, promoting reduction of CRAL into CROL; and/or ii) promote higher CRAL coverage, making the adsorption through C = O favored; or/and even iii) have a higher turnover frequency for CROL production. Aside from the selectivity gains, r-catalysts showed FE's and MB's that are somewhat higher than observed for ur-Au; thus, we can speculate that the reaction pathway toward CROL (reduction of C = O instead of C = C) is less susceptible to side polymerization reactions, or that the reconstructed films have a lower density of sites that catalyze side reactions (e.g., these could happen on defects or higher index facets). Reaction rates also had small improvements with reconstruction, with the most substantial rate gains (factor of 2–3) on surfaces reconstructed by C1SH and C3SH. Given that C1SH and C3SH also had the greatest selectivities toward CROL, this may indicate that the turnover frequency on the sites that favor CROL is slightly higher than that on the sites selective to BuAL—in other words, the selectivity comes from accelerating CROL formation more than from suppressing BuAL formation.

4. Conclusions

The catalytic behaviors of thiol-free polycrystalline Au catalysts subjected to SAM-induced reconstruction were studied by different electrochemical probes: Pb underpotential deposition, formic acid oxidation, and reduction of an α,β unsaturated carbonyl compound (crotonaldehyde). Based on Pb-UPD, the reconstruction seems to increase the quantity of (111)-terraces. A simultaneous change in the nature and distribution of defects within all domains was also observed. This complex surface reorganization promoted a slower onset but higher activity for FAOR, and a 20 − 40% shift of CRAL selectivity toward CROL, giving collective evidence that this effect may have a significant contribution to the catalytic behaviors of thiol-modified SAM surfaces, whether or not the SAM is removed.

CRediT authorship contribution statement

Francisco W.S. Lucas: Conceptualization, Methodology, Investigation, Writing – original draft, Writing – review & editing. **Nathanael C. Ramos:** Investigation, Writing – review & editing. **Daniel K. Schwartz:** Supervision, Writing – review & editing. **J. Will Medlin:** Supervision, Writing – review & editing. **Adam Holewinski:** Supervision, Conceptualization, Writing – review & editing.

Declaration of Competing Interest

There are no conflicts to declare.

Data availability

Data will be made available on request.

Acknowledgments

The authors acknowledge funding support from the National Science Foundation under CBET grant number 2004090.

Supplementary materials

Supplementary material associated with this article can be found, in the online version, at doi:10.1016/j.electacta.2023.142586.

References

[1] C. Vericat, M.E. Vela, G. Corthey, E. Pensa, E. Cortés, M.H. Fonticelli, F. Ibañez, G. E. Benitez, P. Carro, R.C. Salvarezza, Self-Assembled Monolayers of Thiolates on Metals: a Review Article on Sulfur-Metal Chemistry and Surface Structures, RSC Adv. 4 (53) (2014) 27730–27754, https://doi.org/10.1039/C4RA04659E.

[2] J.C. Love, L.A. Estroff, J.K. Kriebel, R.G. Nuzzo, G.M. Whitesides, Self-assembled monolayers of thiolates on metals as a form of nanotechnology, Chem. Rev. 105 (4) (2005) 1103–1170, https://doi.org/10.1021/cr0300789.

[3] M. Makosch, W.-.I. Lin, V. Bumbálek, J. Sá, J.W. Medlin, K. Hungerbühler, J.A. van Bokhoven, Organic thiol modified Pt/TiO $_2$ catalysts to control chemoselective hydrogenation of substituted nitroarenes, ACS Catal. 2 (10) (2012) 2079–2081, https://doi.org/10.1021/cs300378p.

[4] J.M. Hermann, H. Müller, L. Daccache, C. Adler, S. Keller, M. Metzler, T. Jacob, L. A. Kibler, Formic acid oxidation reaction on Au(111) electrodes modified with 4-mercaptopyridine SAM, Electrochim. Acta 388 (2021), 138547, https://doi.org/10.1016/j.electacta.2021.138547.

[5] C. Du, C. Qiu, Z. Fang, P. Li, Y. Gao, J. Wang, W. Chen, Interface hydrophobic tunnel engineering: a general strategy to boost electrochemical conversion of N2 to NH3, Nano Energy 92 (2022), 106784, https://doi.org/10.1016/j.nanoen.2021.106784.

[6] J. Wang, F. Zhang, X. Kang, S. Chen, Organic functionalization of metal catalysts: enhanced activity towards electroreduction of carbon dioxide, Curr. Opin. Electrochem. 13 (2019) 40–46, https://doi.org/10.1016/j.coelec.2018.10.010.

[7] D. Wakerley, S. Lamaison, F. Ozanam, N. Menguy, D. Mercier, P. Marcus, M. Fontecave, V. Mougel, Bio-inspired hydrophobicity promotes CO2 reduction on a Cu surface, Nat. Mater. 18 (11) (2019) 1222–1227, https://doi.org/10.1038/s41563-019-0445-x.

[8] Y. Fang, X. Cheng, J.C. Flake, Y. Xu, CO $_2$ electrochemical reduction at thiolate-modified bulk Au electrodes, Catal. Sci. Technol. 9 (10) (2019) 2689–2701, https://doi.org/10.1039/C9CY00506D.

[9] G. Iijima, H. Yamaguchi, T. Inomata, H. Yoto, M. Ito, H. Masuda, Methanethiol SAMs induce reconstruction and formation of Cu $^+$ on a Cu catalyst under electrochemical CO_2 reduction, ACS Catal. 10 (24) (2020) 15238–15249, https://doi.org/10.1021/acscatal.0c04106.

[10] L. Tang, F. Li, W. Zhou, Q. Guo, The Structure of methylthiolate and ethylthiolate monolayers on Au(111): absence of the $(\sqrt{3} \times \sqrt{3})R30^\circ$ phase, Surf. Sci. 606 (5–6) (2012) L31–L35, https://doi.org/10.1016/j.susc.2011.12.005.

[11] M. Yu, N. Bovet, C.J. Satterley, S. Bengió, K.R.J. Lovelock, P.K. Milligan, R. G. Jones, D.P. Woodruff, V. Dhanak, True nature of an archetypal self-assembly system: mobile Au-thiolate species on Au(111), Phys. Rev. Lett. 97 (16) (2006), 166102, https://doi.org/10.1103/PhysRevLett.97.166102.

[12] Y. Liu, V. Ozolins, Self-assembled monolayers on Au(111): structure, energetics, and mechanism of reconstruction lifting, J. Phys. Chem. C 116 (7) (2012) 4738–4747, https://doi.org/10.1021/jp211407p.

[13] P. Carro, E. Pensa, C. Vericat, R.C. Salvarezza, Hydrocarbon chain length induces surface structure transitions in alkanethiolate–gold adatom self-assembled monolayers on Au(111), J. Phys. Chem. C 117 (5) (2013) 2160–2165, https://doi.org/10.1021/jp310800e.

[14] E. Pensa, P. Carro, A.A. Rubert, G. Benítez, C. Vericat, R.C. Salvarezza, Thiol with an unusual adsorption−desorption behavior: 6-mercaptopurine on Au(111), Langmuir 26 (22) (2010) 17068–17074, https://doi.org/10.1021/la102441b.

[15] G.E. Poirier, Mechanism of formation of Au vacancy Islands in Alkanethiol monolayers on Au(111), Langmuir 13 (7) (1997) 2019–2026, https://doi.org/10.1021/la960777z.

[16] P. Maksymovych, J.T. Yates, Au adatoms in self-assembly of benzenethiol on the Au(111) surface, J. Am. Chem. Soc. 130 (24) (2008) 7518–7519, https://doi.org/10.1021/ja800577w.

[17] E.A. Ramírez, E. Cortés, A.A. Rubert, P. Carro, G. Benítez, M.E. Vela, R. C. Salvarezza, Complex surface chemistry of 4-mercaptopyridine self-assembled monolayers on Au(111), Langmuir 28 (17) (2012) 6839–6847, https://doi.org/10.1021/la204951u.

[18] M.T. Räisänen, M. Kemell, M. Leskelä, T Repo, Oxidation of elemental gold in alcohol solutions, Inorg. Chem. 46 (8) (2007) 3251–3256, https://doi.org/10.1021/ic0624468.

[19] G. Pieters, L.J. Prins, Catalytic self-assembled monolayers on gold nanoparticles, New J. Chem. 36 (10) (2012) 1931, https://doi.org/10.1039/c2nj40424a.

[20] S.H. Pang, C.A. Schoenbaum, D.K. Schwartz, J.W. Medlin, Effects of thiol modifiers on the kinetics of furfural hydrogenation over Pd catalysts, ACS Catal. 4 (9) (2014) 3123–3131, https://doi.org/10.1021/cs500598y.

[21] K.R. Kahsar, D.K. Schwartz, J.W. Medlin, Selective hydrogenation of polyunsaturated fatty acids using alkanethiol self-assembled monolayer-coated Pd/Al $_2$ O $_3$ catalysts, ACS Catal. 3 (9) (2013) 2041–2044, https://doi.org/10.1021/cs4004563.

[22] S.H. Pang, N.E. Love, J.W. Medlin, Synergistic effects of alloying and thiolate modification in furfural hydrogenation over Cu-based catalysts, J. Phys. Chem. Lett. 5 (23) (2014) 4110–4114, https://doi.org/10.1021/jz502153q.

[23] C.-.H. Lien, J.W. Medlin, Promotion of activity and selectivity by alkanethiol monolayers for Pd-catalyzed benzyl alcohol hydrodeoxygenation, J. Phys. Chem. C 118 (41) (2014) 23783–23789, https://doi.org/10.1021/jp507114g.

[24] K.R. Kahsar, S. Johnson, D.K. Schwartz, J.W. Medlin, Hydrogenation of cinnamaldehyde over Pd/Al2O3 catalysts modified with thiol monolayers, Top. Catal. 57 (17–20) (2014) 1505–1511, https://doi.org/10.1007/s11244-014-0325-1.

[25] K.R. Kahsar, D.K. Schwartz, J.W. Medlin, Control of metal catalyst selectivity through specific noncovalent molecular interactions, J. Am. Chem. Soc. 136 (1) (2014) 520–526, https://doi.org/10.1021/ja411973p.

[26] J. Tkac, J.J. Davis, An optimised electrode pre-treatment for SAM formation on polycrystalline gold, J. Electroanalyt. Chem. 621 (1) (2008) 117–120, https://doi.org/10.1016/j.jelechem.2008.04.010.

[27] D. Hobara, M. Yamamoto, T. Kakiuchi, Reconstruction of Au(111) following the reductive desorption of self-assembled monolayers of 2-mercaptoethanesulfonic

acid studied by in situ scanning tunneling microscopy, Chem. Lett. 30 (4) (2001) 374–375, https://doi.org/10.1246/cl.2001.374.
[28] F.-.S. Li, W. Zhou, Q. Guo, Uncovering the hidden gold atoms in a self-assembled monolayer of alkanethiol molecules on Au(111), Phys. Rev. B 79 (11) (2009), 113412, https://doi.org/10.1103/PhysRevB.79.113412.
[29] Q. Guo, X. Sun, R.E. Palmer, Structural dynamics induced by self-assembled monolayers on Au(111), Phys. Rev. B 71 (3) (2005), 035406, https://doi.org/10.1103/PhysRevB.71.035406.
[30] M. Łukaszewski, Electrochemical methods of real surface area determination of noble metal electrodes – an overview, Int. J. Electrochem. Sci. (2016) 4442–4469, https://doi.org/10.20964/2016.06.71.
[31] C. Jeyabharathi, P. Ahrens, U. Hasse, F Scholz, Identification of low-index crystal planes of polycrystalline gold on the basis of electrochemical oxide layer formation, J. Solid State Electrochem. 20 (11) (2016) 3025–3031, https://doi.org/10.1007/s10008-016-3228-1.
[32] A. Hamelin, J. Lipkowski, Underpotential deposition of lead on gold single crystal faces, J. Electroanal. Chem. Interfacial Electrochem. 171 (1–2) (1984) 317–330, https://doi.org/10.1016/0022-0728(84)80123-0.
[33] X. Yang, Q. Meng, X. Wang, Z. Jin, C. Liu, J. Ge, W. Xing, A new pathway for formic acid electro-oxidation: the electro-chemically decomposed hydrogen as a reaction intermediate, J. Energy Chem. 71 (2022) 188–191, https://doi.org/10.1016/j.jechem.2022.03.036.
[34] N. Ramos, J.W. Medlin, A. Holewinski, Electrochemical stability of thiolate self-assembled monolayers on Au, Pt, and Cu, ACS Appl. Mater. Interfaces 15 (11) (2023) 14470–14480, https://doi.org/10.1021/acsami.3c01224.
[35] E. Herrero, L.J. Buller, H.D. Abruña, Underpotential deposition at single crystal surfaces of Au, Pt, Ag and other materials, Chem. Rev. 101 (7) (2001) 1897–1930, https://doi.org/10.1021/cr9600363.
[36] G.M. Brisard, E. Zenati, H.A. Gasteiger, N. Markovic, P.N. Ross, Underpotential deposition of lead on copper(111): a study using a single-crystal rotating ring disk electrode and ex situ low-energy electron diffraction and scanning tunneling microscopy, Langmuir 11 (6) (1995) 2221–2230, https://doi.org/10.1021/la00006a060.
[37] N.J. Tao, J. Pan, Y. Li, P.I. Oden, J.A. DeRose, S.M. Lindsay, Initial stage of underpotential deposition of pb on reconstructed and unreconstructed Au(111), Surf. Sci. 271 (1–2) (1992) L338–L344, https://doi.org/10.1016/0039-6028(92)90855-Z.
[38] C.H. Chen, N. Washburn, A.A. Gewirth, In situ atomic force microscope study of lead underpotential deposition on gold (111): structural properties of the catalytically active phase, J. Phys. Chem. 97 (38) (1993) 9754–9760, https://doi.org/10.1021/j100140a036.
[39] M.P. Green, K.J. Hanson, R. Carr, I. Lindau, STM observations of the underpotential deposition and stripping of Pb on Au(111) under potential sweep conditions, J. Electrochem. Soc. 137 (11) (1990) 3493–3498, https://doi.org/10.1149/1.2086255.
[40] C. Jeyabharathi, M. Zander, F. Scholz, Underpotential deposition of lead on Quasi-spherical and faceted gold nanoparticles, J. Electroanalyt. Chem. 819 (2018) 159–162, https://doi.org/10.1016/j.jelechem.2017.10.011.
[41] A. Hamelin, Underpotential deposition of lead on single crystal faces of gold, J. Electroanal. Chem. Interfacial Electrochem. 165 (1–2) (1984) 167–180, https://doi.org/10.1016/S0022-0728(84)80095-9.
[42] A. Cuesta, G. Cabello, F.W. Hartl, M. Escudero-Escribano, C. Vaz-Domínguez, L. A. Kibler, M. Osawa, C. Gutiérrez, Electrooxidation of formic acid on gold: an ATR-SEIRAS study of the role of adsorbed formate, Catal. Today 202 (2013) 79–86, https://doi.org/10.1016/j.cattod.2012.04.022.
[43] A. Hamelin, Y. Ho, S.C. Chang, X. Gao, M.J. Weaver, Surface crystallographic dependence of voltammetric oxidation of polyhydric alcohols and related systems at monocrystalline gold-acidic aqueous interfaces, Langmuir 8 (3) (1992) 975–981, https://doi.org/10.1021/la00039a038.
[44] S. Liu, T. Ishimoto, M. Koyama, First-principles calculation of OH^-/OH adsorption on gold nanoparticles, Int. J. Quantum Chem. 115 (22) (2015) 1597–1605, https://doi.org/10.1002/qua.24989.
[45] S. Beyhan, K. Uosaki, J.M. Feliu, E. Herrero, Electrochemical and in situ FTIR studies of ethanol adsorption and oxidation on gold single crystal electrodes in alkaline media, J. Electroanalyt. Chem. 707 (2013) 89–94, https://doi.org/10.1016/j.jelechem.2013.08.034.
[46] L.R.L. Ting, Y. Peng, B.S. Yeo, Mechanistic insights into the selective electroreduction of crotonaldehyde to crotyl alcohol and 1-butanol, ChemSusChem 14 (14) (2021) 2963–2971, https://doi.org/10.1002/cssc.202100513.
[47] Z.J. Barton, G.H. Garrett, N. Kurtyka, T.D. Spivey, J.A. Schaidle, A. Holewinski, Electrochemical reduction selectivity of crotonaldehyde on copper, J. Appl. Electrochem. 51 (1) (2021) 5–17, https://doi.org/10.1007/s10800-020-01415-2.
[48] F.W.S. Lucas, R.G. Grim, S.A. Tacey, C.A. Downes, J. Hasse, A.M. Roman, C. A. Farberow, J.A. Schaidle, A. Holewinski, Electrochemical routes for the valorization of biomass-derived feedstocks: from chemistry to application, ACS Energy Lett. 6 (4) (2021) 1205–1270, https://doi.org/10.1021/acsenergylett.0c02692.
[49] W. Liu, Y. Jiang, K.-.H. Dostert, C.P. O'Brien, W. Riedel, A. Savara, S. Schauermann, A. Tkatchenko, Catalysis beyond frontier molecular orbitals: selectivity in partial hydrogenation of multi-unsaturated hydrocarbons on metal catalysts, Sci. Adv. 3 (7) (2017), e1700939, https://doi.org/10.1126/sciadv.1700939.
[50] T.D. Spivey, A. Holewinski, Selective interactions between free-atom-like d-states in single-atom alloy catalysts and near-frontier molecular orbitals, J. Am. Chem. Soc. 143 (31) (2021) 11897–11902, https://doi.org/10.1021/jacs.1c04234.